High-speed chemical imaging of dynamic and histological samples with stimulated Raman micro-spectroscopy

Xavier Audier, Nicolas Forget, Herve Rigneault

Research Article | Vol. 28, No. 10 / 11 May 2020 / Optics Express 15505

Optics EXPRESS

High-speed chemical imaging of dynamic and histological samples with stimulated Raman micro-spectroscopy

XAVIER AUDIER,[1] NICOLAS FORGET,[2] AND HERVÉ RIGNEAULT[1,*]

[1]Aix Marseille Univ, CNRS, Centrale Marseille, Institut Fresnel, 13013 Marseille, France
[2]FASTLITE, 06560 Valbonne, France
[*]herve.rigneault@fresnel.fr

Abstract: We report a shot noise limited high-speed stimulated Raman microscopy platform allowing to acquire molecular vibrational spectra over 200 cm^{-1} in 12 µs at a scan rate of 40kHz. Using spectral focusing together with optimized acousto-optics programmable dispersive filters, the designed low noise imaging platform performs chemical imaging of dynamical processes such as Mannitol crystal hydration and reaches a signal to noise ratio sufficient to perform label free histological imaging on frozen human colon tissue slides.

1. Introduction

Stimulated Raman scattering (SRS) [1] imaging has gain tremendous interest over the last decade due to its ability to perform label free chemical imaging in biological sample [2,3]. In SRS microscopy two laser pulses, a pump at frequency ω_p and a Stokes at frequency ω_s, are focused on a sample to generate an image by point scanning. If the frequency difference $\omega_p - \omega_s$ equals a molecular vibrational frequency Ω_R an energy transfer occurs between the pump and the Stokes beam [4] that can be detected using dedicated modulation schemes. Since SRS imaging first demonstrations [5,6], efforts have been pursue to perform fast images [7], but also to acquire a complete vibrational spectrum at each pixel [8–16]. The fastest approaches to acquire a full spectrum [11,12] use the SRS spectral focusing scheme that allow to retrieve spectral resolution by adding dispersion on the femtosecond pulses [17,18]. When the pump and Stokes pulses are identically chirped, a narrow wavenumber range can be probed within the spectral bandwidth allowed by the pulses (Fig. 1(d)). Not only is spectral resolution recovered, but the probed wavenumber can easily be tuned by adjusting the time delay between the two pulses, allowing for spectral scanning without the need to change the lasers center wavelengths or fast spectrometer. Recently, acousto-optic programmable dispersive filters (AOPDF) have been used as ultrafast delay lines in different applications, such as transient absorption and terahertz spectroscopy [19,20]. Contemporary to this work, spectral focusing and AOPDF has been combined to rapidly sweep the delay between two chirped femtosecond pulses in an SRS microscope [21]. Raman spectra covering the full lipid band (2800 to 3050 cm^{-1}) were acquired at 33 µs per pixel, with a 25 cm^{-1} resolution. Although it showed impressive results, this study did not fully explore the possibilities offered by the technique. In particular, the noise brought by the AOPDF was not studied, the sensitivity was not showcased on biological tissues, and the increased acquisition rate was not applied to the study of chemically dynamic behaviors, while those two aspects are essential for applications.

Here, we report hyperspectral SRS imaging over 200 cm^{-1} in 12 µs at a scan rate of 40kHz with shot noise limited sensitivity. By characterizing the noise in our system and engineering the optimal laser pulses, we have designed an SRS imaging platform combining spectral focusing together with a faster AOPDF delay line to surpass the acquisition speed and sensitivity

#390850 https://doi.org/10.1364/OE.390850
Journal © 2020 Received 3 Mar 2020; revised 23 Apr 2020; accepted 28 Apr 2020; published 7 May 2020

Optics EXPRESS

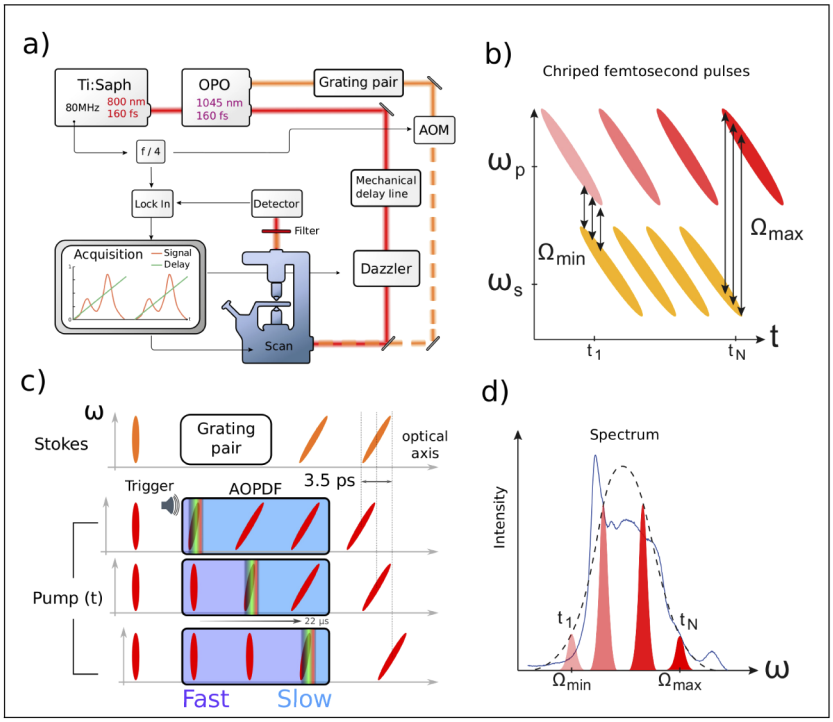

Fig. 1. a) Setup schematics, OPO: optical parametric oscillator, AOM: acousto-optic modulator. b) Spectral focusing scheme: the instantaneous frequency difference between the pulses is a function of the pulses relative delay. c) Acousto-optic programmable dispersive filter (AOPDF): the acoustic wave propagating inside the crystal imprints both negative dispersion, and a delay that changes linearly with the acoustic wave propagation time. d) Schematic of a typical spectrum (solid line) and the spectral bands (red gaussians) probed by the successive chirped pulses illustrated in b). The dashed line represent their relative signal amplitude, and consequently the bandwidth of the system.

demonstrated previously. We demonstrate optimized speed and sensitivity by targeting two major applications that are dynamic chemical imaging and label-free histology on human tissue samples.

2. Setup description

The SRS pump and Stokes beams are generated by a commercial femtosecond laser system (Chameleon OPO-VIS, Coherent) working at 80 MHz repetition rate. (Fig. 1(a)) The pump (800 nm) and Stokes (1045 nm) optical pulses are synchronized, and both can be modeled as Gaussian pulses with temporal full widths at half maximum of 160 fs. The pump laser is sent to an AOPDF (HR or WB Dazzler, Fastlite) which acts as both a tunable dispersive medium and an ultra fast delay line (see details below). The Stokes laser is sent through an acousto-optic modulator (MT200-A0.2-1064, AA optoelectronics) driven by a sinusoidal modulation at one fourth of the laser repetition rate (20 MHz). The first diffraction order of the Stokes beam is collected and sent through a double pass grating pair (custom gratings, Wasatch Photonics) where it undergoes negative dispersion. The modulated and negatively chirped Stokes beam is then recombined with the pump beam by means of a dichroic mirror before being sent to an inverted scanning microscope (TiU, Nikon). The two lasers are focused in the sample using a 20x air objective (0.75NA, CFI Plan Apo Lambda, Nikon) and collected with the same objective in the forward

Optics EXPRESS

direction. The Stokes beam is filtered out using an optical short pass filter (FES0900, Thorlabs), and the pump is collected using a photodiode who's output is then fed to a lock-in amplifier module. The photodiode, the lock-in amplifier and frequency divider are commercial systems optimized to work at 20 MHz (SRS Lockin Module, APE). The lock-in amplifier bandwidth was reduced to 1.35 MHz using an electronic lowpass filter (EF508 Thorlabs, 5th order). The signal from the lock-in was sent to a data acquisition card (ATS460, AlazarTech) and acquired with a sampling rate of 20 MHz. Simultaneously to SRS, and to address biological applications, second harmonic generation (SHG) was recorded at 400 nm in the epi direction, using a dichroic mirror (770dcxr, Chroma) band-pass filter (HQ400/40, Chroma), and photomultiplier tube (R9110 tube and C7950 data socket, Hamamatsu). Average laser powers at the sample plane were 15 mW and 20 mW for the pump and Stokes beams, respectively.

3. AOPDF description

The AOPDF consists of a birefringent crystal in which an acoustic shearing wave co-propagates with an ordinary-polarized optical beam (fast axis). Each acoustic frequency interacts with a specific optical frequency (acousto-optic phase-matching relationship) and gives rise to an extraordinary-polarized diffracted beam (slow axis). Therefore, using the proper acoustic waveform, one can imprint an arbitrary phase profile on incoming optical pulses [22]. In addition to this tunable phase profile, the propagation of the acoustic wave inside the crystal effectively imprints a delay on successive optical pulses that increases linearly over time (Fig. 1(c)). Using both of these properties, one can address the two requirements for spectral focusing SRS: chirped optical pulses and fast delay scanning. Two different AOPDF, the High-Resolution (HR) and Wide-Band (WB), have been used in this study. They are based on the same concept, but have different working parameters, reported in Table 1. In particular, the WB model has a higher repetition rate, a higher diffraction efficiency, and a shorter delay range, making it better suited for the present application. The transmission efficiency of the AOPDF depends on many parameters such as the amount of dispersion added or pulse bandwidth, but ranges from 30% to 60%.

Table 1. Characteristics of the two AOPDF types. Both models consist of a 25-mm-long TeO_2 crystal, but the cut angle is different for each, to allow for different acoustic propagation speed. The repetition rate is the maximum rate at which successive acoustic wave can be sent inside the crystal. The range is the maximum delay allowed by the optical index difference between the fast and slow axis, the values are given for 800 nm light. The time ratio gives the amount of delay added per microsecond of acoustic propagation.

Model	Rep. rate (kHz)	Range (ps)	Ratio (fs/ µs)
HR	30.6	8.5	260
WB	40	3.5	161

4. Noise levels

The laser system used in this study is shot noise limited for electronic frequencies around 20 MHz and average laser intensities at least up to 70 mW [23]. However, to investigate if the AOPDF introduces additional noise, we measure the laser noise in the presence of the AOPDF, at the detector plane, using 5 mW of average laser power and a commercial photodiode (Det10A, 350 MHz bandwidth, Thorlabs). The photodiode was loaded with a 50 Ω resistor and the resulting voltage was filtered with a 5.6 MHz high-pass filter (EF515, 6th order, Thorlabs). The purpose of this filter is to damp the repetition rate and harmonics of the AOPDF (Table 1). The filtered photodiode output was sent to a spectrum analyzer (HF2LI, Zurich instrument) and its electrical power spectral density was acquired between 8 MHz and 40 MHz (Fig. 2(a)).

The power spectral density associated with shot noise is estimated at -191 dB W Hz^{-1}, which is below the detection limit of our spectrum analyzer (-180 dB W Hz^{-1}). However, the laser

Optics EXPRESS

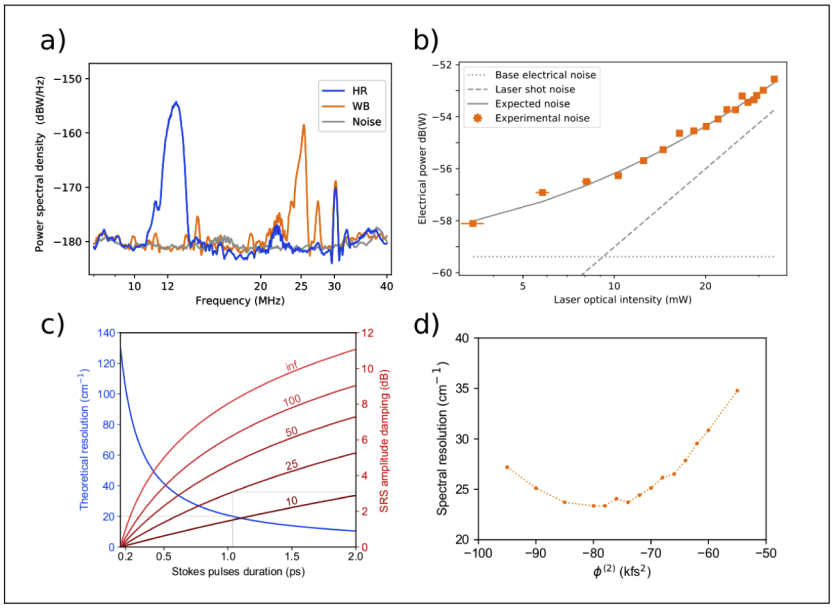

Fig. 2. a) Laser intensity noise for the HR and WB AOPDF. b) System output noise power compared to shot noise and electronic noise, for increasing laser power. c) SRS signal loss and resolution gain as a function of the chirped Stokes pulse duration. The different losses (red lines) corresponds to different linewidths for the probed molecular vibration, indicated in red in cm^{-1}. d) Achieved spectral resolution as a function of the dispersion (second order phase) applied using the AOPDF.

intensity noise introduced by the AOPDF was high enough to be measured without amplification. The laser intensity noise is particularly high around 12 MHz for the HR AOPDF, and around 25 MHz for the WB AOPDF. This point has not been addressed in previous studies, and may have limited the sensitivity of previous systems using these devices. It is suspected that the amplitude noise imprinted on the laser by the AOPDF results from the interference of successive acoustic waves by reflection and diffusion inside the crystal. The carrier frequency for the HR and WB crystals are around 86 MHz and 52.5 MHz respectively. Interactions of the light pulse with co-propagating and counter-propagating acoustic waves may result in optical modulation at double the carrier frequency. Combined with the repetition rate of the laser 80 MHz, this may result in optical modulation at $2 \times 86 - 2 \times 80 = 12$ MHz and $2 \times 52.5 - 80 = 25$ MHz for the HR and WB crystal respectively. To support this hypothesis we mitigated the spatio-temporal overlap of co-propagating and counter-propagating acoustic waves by adding 1 to 5 µs of delay between successive acoustic waves. This did not affect the diffraction efficiency by a significant amount but decreased the recorded noise level to a negligible amount. Although further investigation would be required to fully confirm the origin of the noise, its strong timing sensitivity strongly supports an interaction with counter-propagating acoustic waves, and a 3 µs delay was found enough to decrease the noise to a negligible level.

It is also possible to avoid the excess noise introduced by the AOPDF by selecting a suitable modulation frequency and lock-in bandwidth. Using the lock-in system described previously, with a modulation frequency of 20 MHz and a 1.35 MHz bandwidth, the measured noise from this system matches exactly the expected shot noise from the laser (Fig. 2(b)). For average laser intensities above 9 mW, detector electronic noise becomes negligible compared to the laser shot noise.

Optics EXPRESS

5. Resolution and signal level

Spectral focusing is used to recover spectral resolution when performing SRS with two femtosecond pulses, as illustrated in Fig. 1(b). The spectral resolution that can be achieved using spectral focusing is only a function of the dispersion added to the optical pulses (Fig. 2(c)), and can be improved to less than 5 cm^{-1} with pulses stretched to more than 5 ps. While high spectral resolution may be required for specific applications or in the Raman fingerprint region, the spectral features of interest in dilute samples such as biological tissues that are typically larger than 20 cm^{-1} in the C-H region. Any excessive dispersion does not contribute to significantly improve the resolution of those features, but greatly diminish the amplitude of the SRS signal. As shown in Fig. 2(c), the damping of the SRS signal increases significantly with higher resolution, and a trade-off needs to be made between resolution and signal power. The associated mathematical derivations can be found in the work of Su and collaborators [24].

To optimize the signal/resolution trade-off when imaging biological sample, both pump and Stokes pulses were chirped to 1 ps, by adding negative dispersion with the AOPDF and grating pair, respectively. Such pulse dispersion corresponds to a theoretical value of 22 cm^{-1} for the SRS spectral resolution, and a 3 dB drop in SRS signal assuming sample linewidths of 25 cm^{-1} (Fig. 2(c)).

The AOPDF working range (Table 1) sets the limit on how much dispersion and dispersion can be applied with the device. The acoustic wave needs to be fully formed inside the crystal to achieve the expected resolution, and then propagate to apply the expected delay. As a result, when using the AOPDF for both dispersion and delay, the maximum duration of the pulse allowed by the device is around half of its working range.

The resolution of the spectral measurement was quantified using the Raman line of DMSO at 2913 cm^{-1} (Fig. 2(d)). The amount of dispersion applied on the Stokes pulse with the grating pair was fixed to achieve a 1 ps pulse at the sample plane, measured with an optical autocorrelator (pulseCheck, APE). The amount of added second order phase imprinted on the pump pulse by the AOPDF was optimized (Fig. 2(d)) to match that of the pump pulse, and a resolution of 23 cm^{-1} was achieved. The resulting total negative dispersion is consistent with the optics in the system. The −77 kfs2 second order phase added by the AOPDF includes the −59 kfs2 required to negatively chirp the pulses at the sample plane, the −13 kfs2 required to compensate the dispersion introduced by the AOPDF crystal, and the −5 kfs2 compensating the rest of the optics on the optical path. Higher order dispersion on the pump pulse can be controlled with the AOPDF as well, but the optimal values found were similar to the factory settings for compensating the dispersion inside the AOPDF crystal. We suspect that the 1 cm^{-1} discrepancy between theoretical and experimental resolution may instead be due to the third order dispersion on the Stokes pulse coming from the AOM, grating pair, and lenses.

6. Chemical imaging of multiple species

Figure 3(a) shows the SRS spectra acquired for 5 pure species: melamine (Resin, bead 5um), polystyrene (PS, bead 20um), polymethylmethacrylate (PMMA, bead 10um), bovine serum albumin (BSA) crystals an olive oil solution. An artificial sample composed of these 5 species was prepared and imaged using the WB AOPDF using a pixel dwell time of 25 µs that allowed to record the full Raman spectrum between 2850 cm^{-1} and 3000 cm^{-1} with a resolution ≈23 cm^{-1}. The recorded hyperspectral image was projected over the known pure spectra using linear decomposition that allowed to map the 5 species (Fig. 3(b)). The different components are easily distinguishable without further averaging.

Optics EXPRESS

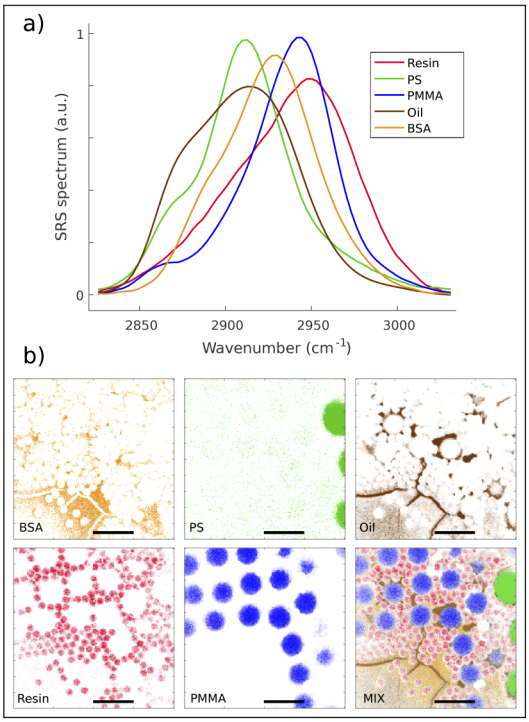

Fig. 3. a) SRS spectra of pure species acquired with the AOPDF delay line (Resin: melamine, PS: polystyrene, PMMA: polymethylmethacrylate, Oil: olive oil, BSA: bovine serum albumin). b) Image components associated with each pure species, as extracted from the hyperspectral image. MIX represents the summed image of all components. Pixel dwell time 25 µs, scale bar: 25 µm, total image acquisition time: 1s

7. Dynamic imaging of chemical reactions

We use here our fast SRS imaging platform to monitor the dynamic of chemical reactions. We concentrate on Mannitol, a common excipient used in pharmaceutical industry, that can crystallize in several polymorphic forms: α, β, and δ. The δ polymorph can change into β upon hydration, and both forms can be identified through their Raman spectra in the lipid band. Understanding how a pharmaceutical compound evolves after ingestion (change in pH and hydration) is key for proper drug delivery. Additionally, the signal levels obtained on Mannitol crystals are comparable to that of lipids in biological samples. The polymorphism of Mannitol is therefore a convenient proxy to the study lipid metabolism, while providing more experimental control than an *in vivo* experiment.

Pure δ-Mannitol crystals were prepared between a microscope slide and a coverslip and imaged over twenty minutes during the introduction of water vapor. Snapshots of the user interface during the acquisition are displayed in Fig. 4.(a-d), while the full video recording is available (Visualization 1). Another example is shown in Visualization 2. δ-Mannitol (red) transforms in β-Mannitol (blue) over time upon water hydratation. We used the HR AOPDF with a frame rate of 1 image every 1.6 second (two successive images were averaged to increase the signal to noise ratio). The hyperspectral images were processed on the fly by projecting them on the components corresponding to pure β and δ-Mannitol (Fig. 4.e), therefore providing live feedback on the crystal transformation process. Because of the dynamic nature of the process, image

Optics EXPRESS

refocusing and tracking of the relevant feature was necessary, and was made possible with live two color rendering.

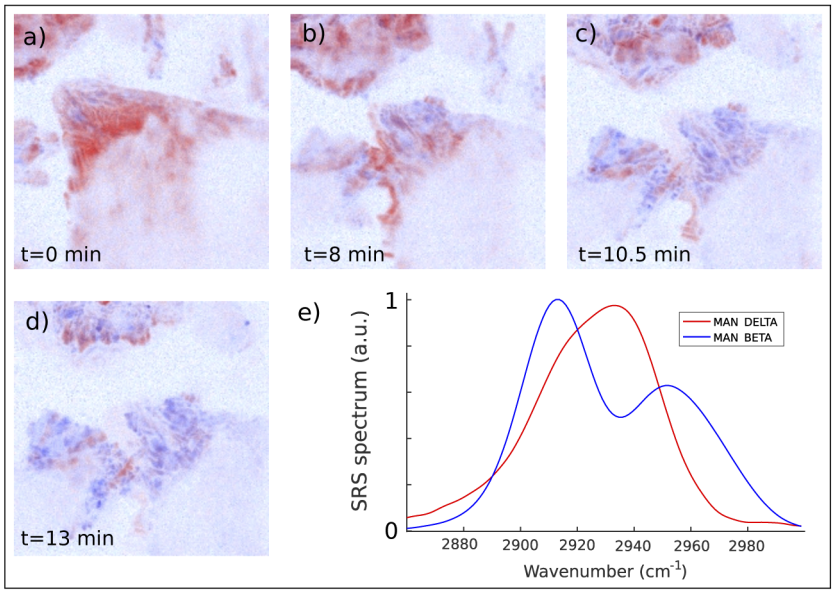

Fig. 4. a)-d) Timelapse of a δ-Mannitol (red) crystal transforming into β-Mannitol (blue) in the contact of water vapour. The field of view is 100 micron large, pixel dwell time 40 µs, e) SRS spectra of pure δ-Mannitol (red) and β-Mannitol (blue).

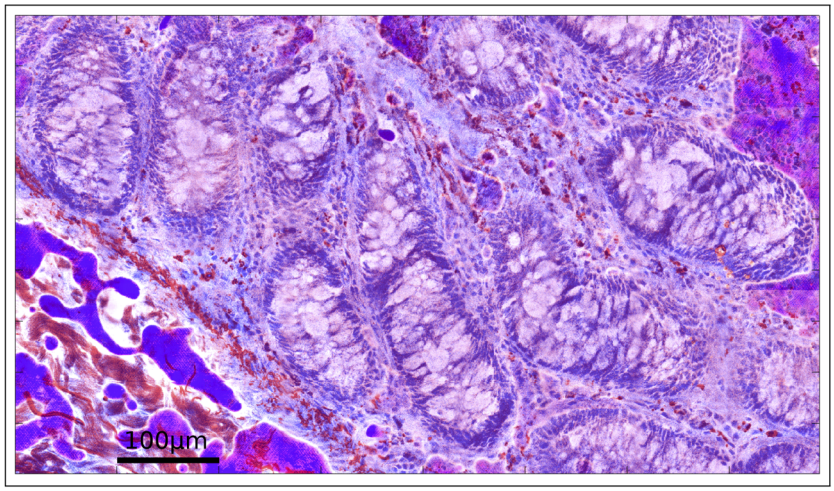

Fig. 5. Frozen section of healthy human colon imaged using fast SRS and SHG. The spatial map of proteins (blue) and lipids (pink), were retrieved using the spectra of BSA and Oil for projection. The SHG signal, characteristic of collagen fibers is shown in red. Image total acquisition time 15 minutes.

Optics EXPRESS

8. Label-free histological recordings

Fast label free imaging of biopsy sections is a major application of coherent Raman imaging that can potentially revolutionize the field of histology by increasing diagnosis speed, lowering hospital costs, and improving patient care [25]. Frozen sections of human cancer colon tissues were imaged with our fast SRS imaging platform, using the WB AOPDF with a pixel time of 25 µs. 8 by 10 adjacent fields of views (100 µm x 100 µm) were acquired separately and stitched together to reconstruct a wider image (Fig. 5). The total acquisition time was 15 minutes. Second harmonic generation at 400 nm was recorded in the epi direction, to provide an additional contrast mechanism specific to collagen fibers. As previously for each pixel, the recorded hyperspectral images were projected on the spectra corresponding to pure BSA (protein) and oil (lipid) to highlight the nuclei and cell bodies, respectively. For rendering look up tables were adjusted to mimic eosin, saffron and haematoxylin staining [26–28].

9. Discussion

Our SRS imaging platform acquires a full vibrational spectra over the [2850 cm^{-1}, 3050 cm^{-1}] spectral range in 12.5 µs, this corresponds to the time during which the chirped pump and Stokes pulses overlapped, while the pump pulse delay is swept by the AOPDF. However the minimum total time per pixel is 25 µs when using the WB AOPDF corresponding to a duty cycle of 50 percent. This figure could be increased by designing a shorter AODPF delay line optimized for lower delay range and higher repetition rate. Using a crystal of only half of the WB crystal length would satisfy both requirements. By applying the second order dispersion with a grating pair, and using the AOPDF solely as a delay line, a 80 kHz pixel acquisition rate should be achievable while maintaining a linear delay sweep. Although such AOPDF hasn't been manufactured, for lack of market application so far, there is not technological barrier to achieving such repetition rate.

The spectral window covered by the system is 200 cm^{-1}, limited by the spectral of the pulses used, which is sufficient to record most of the C-H stretch region. Larger bandwidth could be used by using shorter pulses. We expect the lower limit would be pulses of around 50 µs (at 800 nm). This limit would be set by the difficulty in maintaining phase control and beam wave-front with the dispersive optics used, including the AOPDF, but also the AOM, gratings, and lenses. This limitation is common to most spectral focusing schemes.

Imaging biological tissues (Fig. 5), image-wise averaging had to be performed to achieve signal to noise ratios (SNR) compatible with imaging (SNR > 3 dB). With our shot noise limited system, the SNR achieved on this sample without averaging (pixel dwell time 25 µs) is on the order of 1, corresponding to an associated SRS modulation. $\Delta I/I \approx 2 \times 10^{-5}$.

We limited our investigation to the lipid band but the proposed approach can be easily extended to the fingerprint spectral range using appropriate AOPDF and large bandwidth tunable fs sources. While covering the full fingerprint region using spectral focusing would not be possible due to the dispersive limit detailed above, a window of several hundreds of wave-numbers can still be covered. The narrower features in the fingerprint region would call for pulses dispersed to two or more picosecond. The HR crystal can readily be used for such dispersion and delay scanning. The smaller Raman cross section may limit the acquisition speed significantly, in which case higher Raman signal must be achieved.

This higher signal could be obtained by red-shifting the SRS pump and Stokes wavelength. Using near-infrared light such as 940 nm pump and 1310 nm Stokes, one may significantly increase the average laser power on the sample, while keeping photo-damage low. Such near-IR scheme would allow for an increase of both laser powers by a factor of 2 to 3, which would be sufficient to improve the SNR by a factor of 10, therefore allowing for single SRS spectral measurements per pixel, even on dilute samples or in the Raman fingerprint.

Optics EXPRESS

Other improvements may include the use of spatial multiplexing, provided higher laser powers are available. Using multiple foci has been demonstrated as a method to scale up the acquisition rate [29] in SRS. Another possible strategy would be to use our fast spectral acquisition scheme while under-sampling the image through matrix completion scheme [30]. The amount of data generated by hyperspectral Coherent Raman microscopy can be large, with several hundreds of megabytes per second. The linear delay sweep allowed by the AOPDF simplifies greatly the data processing, which can easily be performed on the fly.

10. Conclusion

We demonstrated fast hyperspectral SRS imaging by combining spectral focusing with an acousto-optic delay line working at 40 kHz. Our system is at the shot noise level for 15 mW of laser probe power, and a bandwidth of 1.3 MHz. The achieved resolution is 23 cm^{-1} over a bandwidth of 130 cm^{-1} full width at half maximum. SRS spectra in the lipid band were acquired with 12.5 µs recordings per pixel corresponding to a duty cycle of 50 percent. Samples containing up to 5 different chemical species have been imaged, and individual component maps were retrieved with no visible cross-talk. Time-resolved imaging of a chemical transformation (δ-Mannitol to β-Mannitol) was made possible, opening the door to other studies requiring fast chemical imaging. Finally, the sensitivity of the system was sufficient to perform stimulated Raman imaging of human frozen tissue sections, demonstrating the applicability of this measurement system for label-free and live histology.

Funding

Agence Nationale de la Recherche (ANR- 10-INSB-04-01, ANR-11-INSB-0006); Institut National de la Santé et de la Recherche Médicale (18CP128-00, PC201508); Aix-Marseille Université (A-M-AAP-ID-17-13-170228-15.22-RIGNEAULT, ANR-11-IDEX-0001-02).

Acknowledgments

The authors thank Barbara Sarri (Institut Fresnel) and Flora Poizat (Institut Paoli-Calmettes) for providing and helping with the frozen tissue sections.

Disclosures

Nicolas Forget has financial interest in FASTLITE.

References

1. N. Bloembergen, "The stimulated Raman effect," Am. J. Phys. **35**(11), 989–1023 (1967).
2. J. X. Cheng and X. S. Xie, "Vibrational spectroscopic imaging of living systems: An emerging platform for biology and medicine," Science **350**(6264), aaa8870 (2015).
3. C. Zhang and J. X. Cheng, "Perspective: Coherent Raman scattering microscopy, the future is bright," APL Photonics **3**(9), 090901 (2018).
4. H. Rigneault and P. Berto, "Tutorial: Coherent Raman light matter interaction processes," APL Photonics **3**(9), 091101 (2018).
5. C. W. Freudiger, W. Min, G. B. Saar, S. Lu, G. R. Holtom, C. He, J. C. Tsai, J. X. Kang, and X. S. Xie, "Label-Free Biomedical Imaging with High Sensitivity by Stimulated Raman Scattering Microscopy," Science **322**(5909), 1857–1861 (2008).
6. P. Nandakumar, A. Kovalev, and A. Volkmer, "Vibrational imaging based on stimulated Raman scattering microscopy," New J. Phys. **11**(3), 033026 (2009).
7. B. G. Saar, C. W. Freudiger, J. Reichman, C. M. Stanley, G. R. Holtom, and X. S. Xie, "Video-Rate Molecular Imaging in Vivo with Stimulated Raman Scattering," Science **330**(6009), 1368–1370 (2010).
8. K. Seto, Y. Okuda, E. Tokunaga, and T. Kobayashi, "Development of a multiplex stimulated raman microscope for spectral imaging through multi-channel lock-in detection," Rev. Sci. Instrum. **84**(8), 083705 (2013).
9. W. Rock, M. Bonn, and S. H. Parekh, "Near shot-noise limited hyperspectral stimulated Raman scattering spectroscopy using low energy lasers and a fast CMOS array," Opt. Express **21**(13), 15113 (2013).

Optics EXPRESS

10. C. S. Liao, M. N. Slipchenko, P. Wang, J. Li, S. Y. Lee, R. A. Oglesbee, and J. X. Cheng, "Microsecond scale vibrational spectroscopic imaging by multiplex stimulated Raman scattering microscopy," Light: Sci. Appl. **4**(3), e265 (2015).
11. C.-S. Liao and J.-X. Cheng, "In Situ and In Vivo Molecular Analysis by Coherent Raman Scattering Microscopy," Annu. Rev. Anal. Chem. **9**(1), 69–93 (2016).
12. R. He, H. Ma, M. Ji, Y. Xu, W. Huang, Z. Liu, R. He, W. Huang, Y. Xu, and Z. Liu, "Stimulated Raman scattering microscopy and spectroscopy with a rapid scanning optical delay line," Opt. Lett. **42**(4), 659–662 (2017).
13. V. Kumar, A. De La Cadena, A. Perri, F. Preda, N. Coluccelli, G. Cerullo, and D. Polli, "Invited Article: Complex vibrational susceptibility by interferometric Fourier transform stimulated Raman scattering," APL Photonics **3**(9), 092403 (2018).
14. B. Figueroa, W. Fu, T. Nguyen, K. Shin, B. Manifold, F. Wise, and D. Fu, "Broadband hyperspectral stimulated raman scattering microscopy with a parabolic fiber amplifier source," Biomed. Opt. Express **9**(12), 6116–6131 (2018).
15. A. Ragni, G. Sciortino, M. Sampietro, G. Ferrari, and D. Polli, "Multi-channel lock-in based differential front-end for broadband raman spectroscopy," Integration **67**, 44–49 (2019).
16. Y. Ozeki, T. Asai, J. Shou, and H. Yoshimi, "Multicolor stimulated raman scattering microscopy with fast wavelength-tunable yb fiber laser," IEEE J. Sel. Top. Quantum Electron. **25**(1), 1–11 (2019).
17. E. Gershgoren, R. Bartels, J. Fourkas, R. Tobey, M. Murnane, and H. Kapteyn, "Simplified setup for high-resolution spectroscopy that uses ultrashort pulses," Opt. Lett. **28**(5), 361–363 (2003).
18. T. Hellerer, A. M. Enejder, and A. Zumbusch, "Spectral focusing: High spectral resolution spectroscopy with broad-bandwidth laser pulses," Appl. Phys. Lett. **85**(1), 25–27 (2004).
19. B. Urbanek, R. Huber, C. Lange, M. Möller, M. Eisele, D. Kaplan, and S. Baierl, "Femtosecond terahertz time-domain spectroscopy at 36 kHz scan rate using an acousto-optic delay," Appl. Phys. Lett. **108**(12), 121101 (2016).
20. X. Audier, N. Balla, and H. Rigneault, "Pump-probe micro-spectroscopy by means of an ultra-fast acousto-optics delay line," Opt. Lett. **42**(2), 294 (2017).
21. M. S. Alshaykh, C.-S. Liao, O. E. Sandoval, G. Gitzinger, N. Forget, D. E. Leaird, J.-X. Cheng, and A. M. Weiner, "High-speed stimulated hyperspectral raman imaging using rapid acousto-optic delay lines," Opt. Lett. **42**(8), 1548–1551 (2017).
22. F. Verluise, V. Laude, J.-P. Huignard, P. Tournois, and A. Migus, "Arbitrary dispersion control of ultrashort optical pulses with acoustic waves," J. Opt. Soc. Am. B **17**(1), 138–145 (2000).
23. X. Audier, S. Heuke, P. Volz, I. Rimke, and H. Rigneault, "Noise in stimulated raman scattering measurement: From basics to practice," APL Photonics **5**(1), 011101 (2020).
24. J. Su, R. Xie, C. K. Johnson, and R. Hui, "Single-fiber-laser-based wavelength tunable excitation for coherent Raman spectroscopy," J. Opt. Soc. Am. B **30**(6), 1671 (2013).
25. M. T. Cicerone and C. H. Camp, "Histological coherent Raman imaging: A prognostic review," Analyst **143**(1), 33–59 (2018).
26. D. A. Orringer, B. Pandian, Y. S. Niknafs, T. C. Hollon, J. Boyle, S. Lewis, M. Garrard, S. L. Hervey-Jumper, H. J. L. Garton, C. O. Maher, J. A. Heth, O. Sagher, D. A. Wilkinson, M. Snuderl, S. Venneti, S. H. Ramkissoon, K. A. McFadden, A. Fisher-Hubbard, A. P. Lieberman, T. D. Johnson, X. S. Xie, J. K. Trautman, C. W. Freudiger, and S. Camelo-Piragua, "Rapid intraoperative histology of unprocessed surgical specimens via fibre-laser-based stimulated raman scattering microscopy," Nat. Biomed. Eng. **1**(2), 0027 (2017).
27. B. Sarri, R. Canonge, X. Audier, E. Simon, J. Wojak, F. Caillol, C. Cador, D. Marguet, F. Poizat, M. Giovannini, and H. Rigneault, "Fast stimulated raman and second harmonic generation imaging for intraoperative gastro-intestinal cancer detection," Sci. Rep. **9**(1), 10052 (2019).
28. B. Sarri, F. Poizat, S. Heuke, J. Wojak, F. Franchi, F. Caillol, M. Giovannini, and H. Rigneault, "Stimulated raman histology: one to one comparison with standard hematoxylin and eosin staining," Biomed. Opt. Express **10**(10), 5378 (2019).
29. H. Rigneault, X. Audier, S. Heuke, B. Sarri, and A. Lombardini, "Dual-focus stimulated Raman scattering microscopy: a concept for multi-focus scaling," Opt. Lett. **43**(19), 4763 (2018).
30. H. Lin, C. S. Liao, P. Wang, N. Kong, and J. X. Cheng, "Spectroscopic stimulated Raman scattering imaging of highly dynamic specimens through matrix completion," Light: Sci. Appl. **7**(5), 17179 (2018).